PTEP

Prog. Theor. Exp. Phys. **2024** 073G01 (19 pages)
DOI: 10.1093/ptep/ptae090

Simple Design Criterion for High-Intensity Hadron Linacs

Asuto Kasagaki and Hiromi Okamoto*

Graduate School of Advanced Science and Engineering, Hiroshima University, 1-3-1 Kagamiyama, Higashi-Hiroshima 739-8530, Japan

*Email: okamoto@sci.hiroshima-u.ac.jp

Received April 15, 2024; Accepted June 13, 2024; Published June 14, 2024

A simple procedure is established to optimize fundamental design parameters of a high-intensity hadron linac where interparticle Coulomb interaction plays a crucial role. Based on the recently proposed semi-empirical resonance condition, a stability map is constructed which reveals potentially dangerous operating regions in tune space. The map is shown to be consistent with numerical data obtained from more complicated approaches. The effectiveness of the new design scheme is demonstrated through systematic particle-in-cell simulations assuming the most typical structure of an Alvarez-type drift tube linac. The present results suggest that the so-called *equipartitioning condition*, which has often been taken very seriously in high-intensity linac designs, does not need to be met to guarantee the best machine performance. The basic design concept described here can be applied not only to linacs but also to circular machines.

Subject Index G06, G10, G11

1. Introduction

The effect of space–charge interaction on beam stability is particularly severe in hadron linacs operating at relatively low energy. This natural mechanism is known to cause serious emittance growth and resultant beam loss in a high-intensity beam injector if the operating condition of the machine is not properly chosen [1,2]. It is, therefore, vital to establish a reliable guideline for the basic design of such machines, including the space-charge effect.

At high density, the motions of individual charged particles forming a dense beam core are no longer independent but rather correlated through the Coulomb self-fields. The collective nature of the whole beam must be taken carefully into consideration to develop an accurate understanding of the beam behavior. Self-consistent theoretical studies conducted in the early 1980s have concluded that the *bare* betatron phase advance $\sigma_\perp$ per alternating-gradient (AG) focusing period must meet the requirement $\sigma_\perp \leq 180^\circ/m$ to eliminate the structure resonance of the mth order in a long AG beam transport channel [3,4]. This criterion has been widely accepted in the community and used for most high-intensity hadron linacs designed thereafter; $\sigma_\perp$ is commonly chosen below 90° to avoid serious linear ($m = 2$) collective resonance. The argument is naturally extended to the longitudinal degree of freedom, setting the same upper limit on the bare synchrotron phase advance $\sigma_\parallel$ per transverse focusing period.

Apart from the upper limit imposed on the phase advances, the concept of the *equipartitioned linac design* was proposed by Jameson [5] and actually applied, e.g. to the proton machines at the Japan Proton Accelerator Research Complex (J-PARC) [6,7]. Hofmann later

derived the dispersion relations of linear and nonlinear collective modes under the smooth approximation, applicable even to anisotropic (nonequipartitioned) beams [8]. Those dispersion relations were solved numerically to describe the stability of space-charge-dominated beams in a uniform channel. The stability diagram, often referred to as the *Hofmann chart*, has been employed as a useful guideline to determine the operating condition of a high-intensity linac [9–14].

In this paper, we propose a new general procedure for designing high-intensity machines. The present design scheme is based on the coherent resonance condition introduced in Sect. 2. The condition, first conjectured in Ref. [15] from a 1D Vlasov theory in Ref. [16], includes only a few free parameters besides the operating bare tunes. We start with a brief review of the 2D case, comparing our theoretical expectations with results of 2D Vlasov analysis. We then outline in Sect. 3 how to draw a new stability chart for coasting beams and also for short bunches typical in linacs. In our approach, dangerous operating regions where the beam may become unstable are displayed in the conventional tune space spanned by the bare phase advances. It is thus easy-to-use and applicable even to circular machines. Self-consistent particle-in-cell (PIC) simulations are performed in Sect. 4, assuming a simple beam transport channel without acceleration. We shall demonstrate that the simulation results can be well understood with the help of our new chart. In Sect. 5, the stability of an intense proton bunch travelling in a drift-tube linac (DTL) of the Alvarez type is explored with PIC simulations and explained by the corresponding stability charts. Finally, we make some concluding remarks in Sect. 6.

2. Semi-empirical condition of coherent betatron resonance

Transverse beam focusing is generally achieved with a periodic array of quadrupole magnets. Owing to this periodic nature of the driving force, the beam becomes resonantly unstable when a certain condition is satisfied by some fundamental machine parameters. If the external driving potential contains a periodic term proportional to $x^{|n_x|}y^{|n_y|}z^{|n_\parallel|}$ with $(n_x, n_y, n_\parallel)$ being integers, the so-called *single-particle resonance* occurs under the condition

$$n_x\sigma_x + n_y\sigma_y + n_\parallel\sigma_\parallel = n360^\circ, \tag{1}$$

where n is another integer, and (σ_x, σ_y) are the bare betatron phase advances in the horizontal (x) and vertical (y) directions [17]. The order of this resonance is $m = |n_x| + |n_y| + |n_\parallel|$. Quadrupole lattice structures adopted for DTLs are usually symmetric with respect to the two transverse directions. The most popular AG lattice is the FODO (Focus-Drift-Defocus-Drift) type, which gives horizontal and vertical phase advances of similar size. In the following discussion, therefore, we assume $\sigma_x = \sigma_y (\equiv \sigma_\perp)$ for the sake of simplicity. Equation (1) is then reduced to

$$n_\perp\sigma_\perp + n_\parallel\sigma_\parallel = n360^\circ, \tag{2}$$

with $n_\perp = n_x + n_y$.

It is evident from the two conditions above that the number of resonance lines increases when $\sigma_x \neq \sigma_y$. If we plot resonance lines, e.g. in the σ_x–$\sigma_\parallel$ plane, many of them will split depending on the value of σ_y. It thus seems practically meaningful to equalize σ_x and σ_y, but such a tune setting is not preferred in rings because of concern that the so-called *Montague resonance* may be excited under the condition $\sigma_x \approx \sigma_y$ [18]. We have, however, verified numerically and even experimentally that the Montague-type resonance can be suppressed by equalizing the beam emittances of the two coupled directions [15,19–21]. In fact, no serious trouble has been

reported in regular DTLs operating with nearly equal horizontal and vertical betatron tunes, even though the beam density is much higher than in rings. Note also that the rapid cycling synchrotron at the J-PARC has achieved very low beam loss of the order of 0.1% with an operating point near the Montague-resonance line [22].

The actual tune of particle oscillation more or less decreases due to interparticle Coulomb repulsion. The effective phase advances are $(\sigma_\perp - \Delta\sigma_\perp, \sigma_\parallel - \Delta\sigma_\parallel)$ rather than $(\sigma_\perp, \sigma_\parallel)$ where the incoherent shifts $(\Delta\sigma_\perp, \Delta\sigma_\parallel)$ become larger at higher beam density. The conventional *incoherent resonance* condition can be obtained by simply replacing $(\sigma_\perp, \sigma_\parallel)$ in Eq. (2) by their effective values:

$$n_\perp(\sigma_\perp - \Delta\sigma_\perp) + n_\parallel(\sigma_\parallel - \Delta\sigma_\parallel) = n360^\circ. \tag{3}$$

This condition has been used in the ring community to explain the beam loss observed in high-intensity synchrotrons and storage rings. The incoherent tune shifts are particle-dependent and thus unobservable. They even depend strongly on the distribution of particles in the beam, so some reasonable distribution function must be assumed to estimate $(\Delta\sigma_\perp, \Delta\sigma_\parallel)$. The Gaussian distribution has been adopted in many cases so far, which defines a necktie-shaped area covered by incoherent phase advances (betatron tunes) of individual particles in transverse tune space.

The incoherent condition as in Eq. (3) is not popular in the linac community. This is, in one sense, interesting because no fundamental difference exists between the two AG systems (linear and circular machines) as far as the basic mechanism of resonance is concerned. The incoherent picture applies only to particles in the beam tail [19–21]. Those tail particles, moving around the dense beam core in six-dimensional phase space, can behave almost independently because of weak Coulomb coupling. The space-charge force from the core can then be treated as a sort of external driving source of resonance in the tail. Such a picture never works in the core region where all particles act collectively. A correct understanding of core dynamics can be reached only through self-consistent investigation.

A pioneering work on space-charge-driven resonance was done by Sacherer, who solved the Vlasov–Poisson equation system for a 1D sheet beam propagating in a uniform focusing channel [23]. Okamoto and Yokoya (OY) later generalized Sacherer's theory, incorporating the periodic nature of beam-focusing lattices [16]. It was found that the *parametric factor* is missing in Sacherer's resonance condition; it takes the form $\Omega_m = n360^\circ$ with Ω_m being the phase advance of the mth-order coherent mode. OY's *coherent resonance* condition can be expressed as $\Omega_m = n360^\circ/2$; the factor "1/2" on the right-hand side gives rise to twice as many resonance stop bands as expected from Sacherer's original prediction.

As the beam density is lowered, Ω_m approaches $m\sigma_\perp$. Since $n = 1$ for a short AG lattice like FODO, Sacherer's formula requires $\sigma_\perp \leq 360^\circ/m$ to eliminate the mth-order structure resonance. This result conflicts with the well-known design criterion of linear AG transport obtained from self-consistent analyses. On the other hand, OY's formula gives $\sigma_\perp \leq 180^\circ/m$, which agrees with the previous conclusion. Only external-field-driven resonances obey the conventional resonance condition without the 1/2; this factor has to be omitted for nonlinear resonances driven by an external source such as error fields in focusing magnets.

In the 2D case, the self-consistent set of equations can be solved only numerically [3,24,25]. It seems hopeless to derive a concise analytic formula mathematically from the Vlasov equation, but based on the 1D formula, the following condition was conjectured for 2D beams [15,19]:

$$n_x\sigma_x[1 - C_m(1 - \eta_x)] + n_y\sigma_y[1 - C_m(1 - \eta_y)] = n'180^\circ, \tag{4}$$

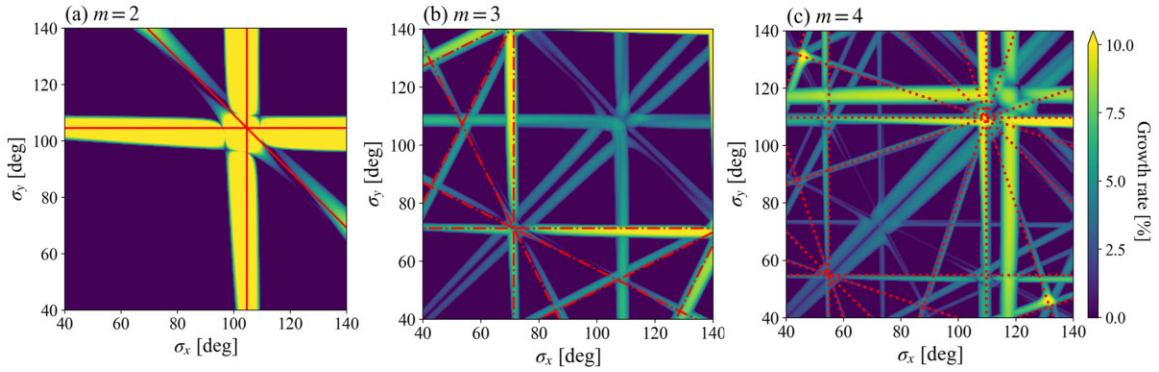

Fig. 1. Coherent instability bands derived from 2D Vlasov analysis with the KV model. The AG lattice assumed here is the standard FODO with a quadrupole occupancy factor of 50%. The rms tune depressions in the horizontal and vertical directions are both fixed at 0.8 over the whole tune space. The three panels show operating regions where emittance growth is expected in the KV core due to the instability of (a) the quadrupole mode ($m = 2$), (b) the sextupole mode ($m = 3$), and (c) the octupole mode ($m = 4$). Coherent resonance lines defined by Eq. (4) are drawn in red for the quadrupole (solid), sextupole (dash-dotted), and octupole (dotted) modes.

where n' is an integer, C_m is the coherent tune-shift factor of the mth-order mode, and (η_x, η_y) are the root-mean-squared (rms) tune depressions calculated from the stationary solution of the rms envelope equations [19]. Similarly to the 1D case, error fields can only enhance coherent core resonances with even n', while the Coulomb self-field has a potential to activate all resonances regardless of the parity of n'.

The rms tune shifts in the x and y directions are defined as $\Delta\overline{\sigma}_{x(y)} \equiv (1 - \eta_{x(y)})\sigma_{x(y)}$. Unlike the incoherent tune shifts in Eq. (3), the rms tune depression is insensitive to the detail of the particle distribution and thus usable as a universal measure of space-charge density [26]. It takes a value close to unity at low beam density and converges to zero at the space-charge limit where the beam is Coulomb crystallized. The coherent tune-shift factor C_m is always positive but less than unity. According to Sacherer's 1D theory, we have $C_2 = 0.75$, $C_3 = 0.88$, and $C_4 = 0.92$. A recent 2D simulation study has concluded similar numbers; namely, $C_2 \approx 0.7$, $C_3 \approx 0.8$, and $C_4 \approx 0.9$ [19].

Equation (4) is free from information like the emittance ratio, the degree of anisotropy, the size of the tune split, etc. The condition can be applied to any kind of 2D beams despite its simpleness. In contrast, the original 2D Vlasov analysis done by Hofmann et al. [3] is limited to a coasting beam with equal transverse emittances. Another Vlasov theory published later can handle more general situations, but the lattice periodicity has been smoothed out [8]; a number of instability bands might be overlooked as a result because of the missing parametric factor. An advanced 2D Vlasov theory was developed more recently, which can handle arbitrary initial conditions of a Kapchinsky–Vladimirsky (KV) beam traveling in arbitrary periodic lattices [24,25]. We here make use of this generalized 2D theory to check the validity of our semi-empirical resonance condition.

Figures 1, 2, and 3, all of which have assumed a typical FODO transport channel, show the distributions of low-order resonances obtained from the KV-based Vlasov analysis. The growth rate of instability is color-coded and plotted as a function of bare tunes. In Fig. 1, the rms tune depressions are adjusted to 0.8 ($\eta_x = \eta_y = 0.8$) everywhere in the stability map. The beam intensity and emittances then depend on the operating point. Figure 2 corresponds to

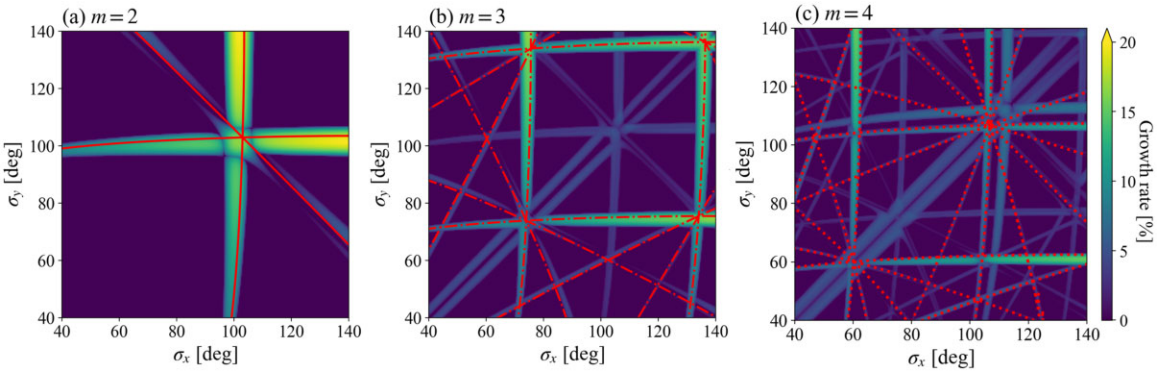

Fig. 2. Coherent instability bands derived from 2D Vlasov analysis with the KV model. The line density and transverse rms emittances of the KV beam have been fixed over the whole tune space at the values that make the transverse rms tune depressions $\eta_{x(y)}$ equal to 0.7 at $(\sigma_x, \sigma_y) = (55^\circ, 55^\circ)$. The beam is assumed to be equipartitioned at this operating point. Other conditions are identical to those assumed in Fig. 1.

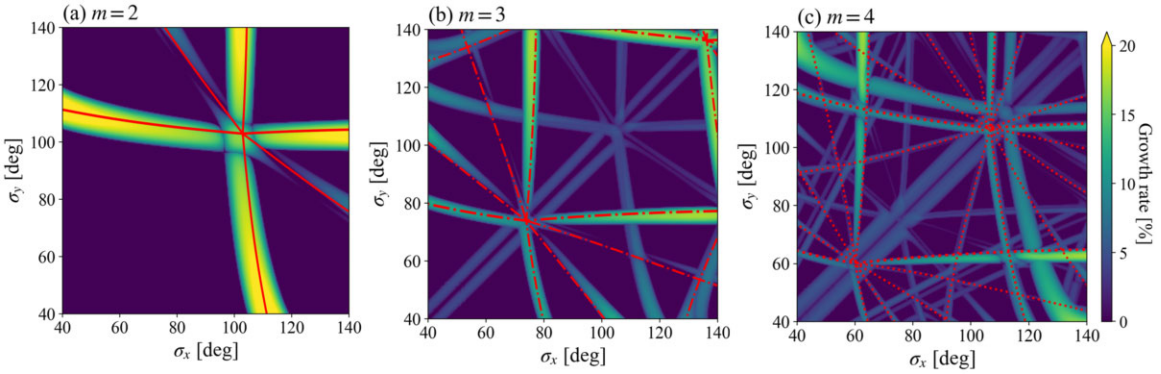

Fig. 3. Coherent instability bands derived from 2D Vlasov analysis with the KV model. The line density of the KV beam is the same as in Fig. 2, but the transverse rms emittances have been changed here such that the equipartitioned state is maintained everywhere. Other conditions are identical to those assumed in Fig. 1.

a more practical situation where the beam intensity and transverse rms emittances are simply maintained regardless of the operating tunes. The intensity is fixed at the value that gives $\eta_x = \eta_y = 0.7$ at $(\sigma_x, \sigma_y) = (55^\circ, 55^\circ)$ where the horizontal and vertical rms emittances $(\varepsilon_x, \varepsilon_y)$ fulfill the so-called *equipartitioning condition* [5]:

$$\frac{\varepsilon_y}{\varepsilon_x} = \frac{\eta_x \sigma_x}{\eta_y \sigma_y}. \tag{5}$$

In Fig. 3, we have set this condition to be satisfied everywhere by optimizing the emittance ratio. The rms tune depressions then become a function of the operating phase advances as depicted in Fig. 4.

The three panels in each figure represent the distributions of coherent instability regions associated with the quadrupole ($m = 2$), sextupole ($m = 3$), and octupole ($m = 4$) modes. We find that the KV-based Vlasov theory predicts many nonlinear stop bands. In the cases of Figs. 2 and 3, the stop bands are curved due to the dependence of the tune depression on the operating point. The red solid, dash-dotted, and dotted lines are the corresponding predictions from Eq. (4) with the coherent tune-shift factors fixed at $C_2 = 0.7$, $C_3 = 0.8$, and $C_4 = 0.9$. In all cases, these lines agree remarkably well with major stop bands obtained by numerical

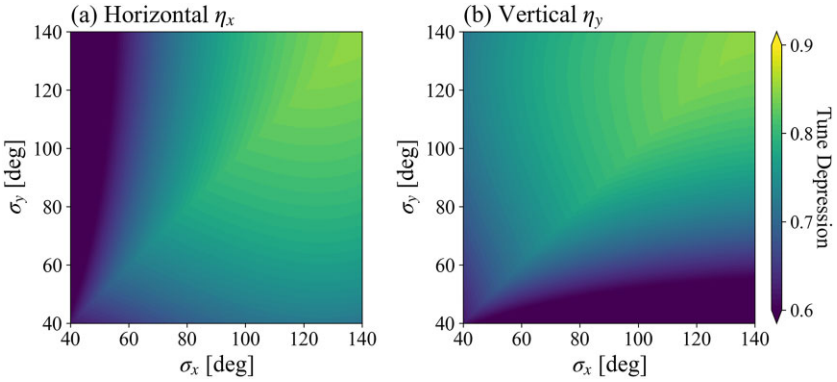

Fig. 4. Operating-point dependence of the rms tune depressions under the condition in Fig. 3.

integration of the complicated coupled differential equations given in Refs. [24,25]. Other stop bands without a red line overlapped are believed to be unimportant in practice or covered by resonances of lower orders. In fact, these unusual stop bands inconsistent with Eq. (4) have no noticeable effect on the beam quality, as demonstrated in previous studies [27,28] and reconfirmed by numerical simulations later. A possible cause for these extra stop bands is the use of an unrealistic distribution like the KV type [29]. The KV beam is known to be intrinsically unstable even in a uniform focusing channel [30]. In addition, the band widths of coherent resonances in the KV beam tend to be narrower than those in realistic particle distributions. This is obvious from the PIC data in Sect. 4 where the Gaussian distribution has been assumed.

We realize that a few resonance lines are missing in the present stability charts; e.g. the linear difference resonance line is invisible in all three cases. According to a finding in Ref. [19], difference resonances of specific n_x and n_y are strongly suppressed if the two emittances fulfill the relation

$$\Lambda(n_x, n_y) \equiv \frac{\varepsilon_x}{n_x} + \frac{\varepsilon_y}{n_y} = 0. \tag{6}$$

The same argument applies to synchrobetatron difference resonances [27]. This is why the transverse Montague resonance is of no concern in most linacs where the horizontal and vertical emittances are roughly equal at injection.

3. Stop-band diagram

The Vlasov formalism contains all physical information about beam stability, except for the effect of interparticle Coulomb collisions. Figures 1, 2, and 3, therefore, offer very accurate information of possible resonances in the KV beam well matched to the FODO lattice. A drawback is, as already remarked above, the appearance of unrealistic (or practically unimportant) stop bands peculiar to the KV-type distribution function. The theory is, however, still useful to check the accuracy of predictions made by an empirical formula like Eq. (4). The numerical results in the last section demonstrate that the locations of major coherent instability bands under any initial beam conditions are predicted well by the proposed resonance formula. Equation (4) can provide us with all-important pieces of information about space-charge-induced instability in a matched hadron beam, thus allowing for quick and reliable optimization of fundamental design parameters of any high-intensity machine.

The 2D formula of betatron resonance can naturally be extended to explore stability issues of intense bunched beams [27]. In the case of symmetric transverse focusing ($\sigma_x = \sigma_y$) adopted

for many linacs, we only need to replace a few parameters in Eq. (4) with those relevant to synchrotron motion:

$$n_\perp \sigma_\perp [1 - C_m(1 - \eta_\perp)] + n_\parallel \sigma_\parallel [1 - C_m(1 - \eta_\parallel)] = n' 180^\circ, \tag{7}$$

where $\eta_\perp$ and $\eta_\parallel$ denote the rms tune depressions in the transverse and longitudinal directions. Equation (7) has a form analogous to standard resonance formulas conventionally used in the accelerator community for many years. The use of this simple formula enables one to visualize dangerous operating conditions easily in the ordinary bare-tune space.

We need to give a certain width to each coherent resonance line defined by Eq. (7). The width of a stop band depends on several conditions such as the lattice design, strengths of external error fields, and even the distribution function of particles. Deriving its precise analytic description for a multidimensional beam is thus extremely difficult; however, based on a finding from 1D Vlasov analysis [16], the following formula has been proposed for a rough estimate of the band width $\delta w(n_\perp, n_\parallel)$ for an arbitrary combination of $n_\perp$ and $n_\parallel$ [21,28]:

$$\delta w(n_\perp, n_\parallel) = 2g(n_\perp, n_\parallel)(1 - C_m)\frac{1 - \overline{\eta}}{\overline{\eta}}\overline{\sigma}, \tag{8}$$

where $\overline{\eta} \equiv (\eta_\perp + \eta_\parallel)/2$, $\overline{\sigma} \equiv (\sigma_\perp + \sigma_\parallel)/2$, and $g(n_\perp, n_\parallel) \equiv |n_\parallel \varepsilon_\perp + n_\perp \varepsilon_\parallel|/(|n_\parallel|\varepsilon_\perp + |n_\perp|\varepsilon_\parallel)$ with $\varepsilon_\perp$ and $\varepsilon_\parallel$ being the transverse and longitudinal rms emittances. Here, we have assumed an equal emittance in the horizontal and vertical directions; i.e. $\varepsilon_x = \varepsilon_y (\equiv \varepsilon_\perp)$. The factor $g(n_\perp, n_\parallel)$ reflects the fact that difference resonances are suppressed under the condition in Eq. (6). Since C_m approaches unity with increasing m, the width of a higher-order resonance becomes narrower.

An incoherent resonance domain, where tail particles may become unstable, lies next to a coherent resonance band [19–21,31]. Each tail particle loses its stability independently of the others under the condition in Eq. (3). Considering the spatial symmetry of a matched beam core formed by the quadratic AG focusing potential, space-charge-driven incoherent resonances should be particularly severe with even $n_\perp$ and even $n_\parallel$. Serious incoherent resonances may thus be excited under the condition

$$2n_\perp(\sigma_\perp - \Delta\sigma_\perp) + 2n_\parallel(\sigma_\parallel - \Delta\sigma_\parallel) = n' 360^\circ. \tag{9}$$

This line is in the vicinity of the coherent resonance line in Eq. (7). In fact, multiplying both sides of Eq. (7) by 2, we have $2n_\perp(\sigma_\perp - C_m\Delta\overline{\sigma}_\perp) + 2n_\parallel(\sigma_\parallel - C_m\Delta\overline{\sigma}_\parallel) = n' 360^\circ$ where $\Delta\overline{\sigma}_{\perp(\parallel)}$ are the rms tune shifts. Since C_m ($m \geq 2$) is always near unity, we understand that incoherent tail resonances under Eq. (9) occur just beside the coherent core resonance along the line defined by Eq. (7). One or both incoherent shifts $\Delta\sigma_{\perp(\parallel)}$ of the tail particles are considerably smaller than the rms shifts $\Delta\overline{\sigma}_{\perp(\parallel)}$, so the tail-resonance region is located on the low-tune side of the neighboring coherent stop band. The order of this incoherent effect is $2m$, twice as high as that of the neighboring coherent resonance.

The quasi-incoherent effect in the beam tail plays an important role especially in circular machines [21,31]. In any synchrotrons and storage rings, the tune depression is generally much closer to unity than in the case of high-intensity linacs. The coherent effect in the beam core is then very weak. In most cases, the instability of a nonlinear coherent mode will be damped spontaneously before causing a detectable level of beam loss, because the resonance-induced emittance growth results in a reduction of the beam density in phase space. The density reduction gives rise to the shift and shrinkage of the stop band, making the operating point escape from the resonance. After that, particle losses, if any, will come largely from the beam tail because the incoherent resonance has no such self-inhibition mechanism.

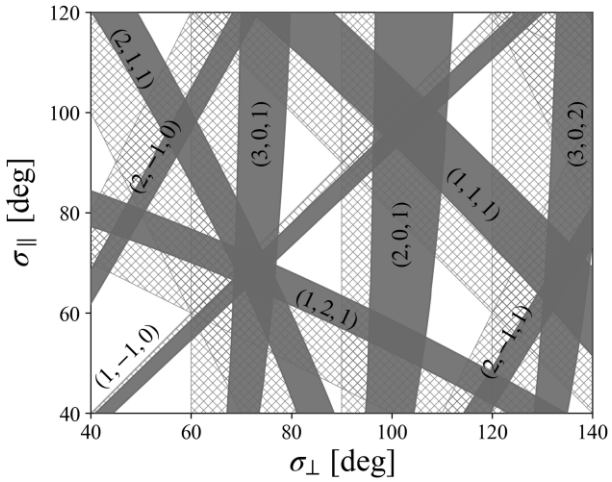

Fig. 5. Stop-band diagram of a nonequipartitioned bunch. The intensity and rms emittances of the bunch are fixed at the values that give $\eta_\perp = 0.8$ at the operating point $(\sigma_\perp, \sigma_\parallel) = (50^\circ, 25^\circ)$. Coherent core resonance bands (shaded area) of the second and third orders are shown together with the domains of accompanying tail resonances (hatched area). The three numbers written beside each band represent $(n_\perp, n_\parallel, n')$ in Eq. (7). The following tune-shift factors have been assumed: $C_2 = 0.7$ and $C_3 = 0.8$.

Employing the coherent resonance condition in Eq. (7) together with the band-width formula in Eq. (8), we can readily draw a stability map in the following way: First, calculate the rms tune depressions in the $\sigma_\perp$–$\sigma_\parallel$ plane by solving the rms envelope equations (see Fig. 4). Once $\eta_{\perp(\parallel)}$ are determined as a function of the bare phase advances, it is straightforward to plot coherent resonance lines given by Eq. (7). An important question is up to what order of resonances we should consider. Our past numerical and experimental experiences suggest that coherent stop bands of at least up to the third order ($m = 3$) must be taken into consideration [19–21]. In linear accelerators, nonlinear collective modes of the fourth and higher orders ($m \geq 4$) probably have no serious impact on beam quality unless the machine is extremely long and/or the beam density is extremely high. After plotting all coherent resonance lines up to a proper order in tune space, give each line a finite width defined by Eq. (8). Finally, identify where particles in the beam tail may become unstable under the condition in Eq. (9). Incoherent resonances in the beam tail are usually expected within the narrow space between the nearby core resonance band and the single-particle resonance line. Tail-resonance domains demand particular care and attention in rings as explained above, but even in linacs they had better be avoided to ensure the best beam quality.

Figure 5 shows a typical stop-band diagram where the intensity and rms emittances of the bunch are kept unchanged regardless of the operating point. The bunch intensity is determined such that the transverse rms tune depression becomes 0.8 at the operating point $(\sigma_\perp, \sigma_\parallel) = (50^\circ, 25^\circ)$. We see several low-order stop bands even in the region $\sigma_{\perp(\parallel)} < 90^\circ$. Those resonances expected in a low-tune range are of the third order, except for the difference resonance with $(n_\perp, n_\parallel, n') = (1, -1, 0)$. The effect of the nonlinear stop bands on the beam quality is believed to be rather limited in ordinary DTLs, but to be on the safe side, it is advisable to avoid all of them.

Note that the difference resonance with $(n_\perp, n_\parallel, n') = (1, -2, 0)$ is missing in Fig. 5. In this diagram, the beam is assumed to be equipartitioned at $(\sigma_\perp, \sigma_\parallel) = (50^\circ, 25^\circ)$. Since $\sigma_\perp/\sigma_\parallel = 2$ there, the emittance ratio $\varepsilon_\perp/\varepsilon_\parallel$ is near 0.5 unless the tune depressions of the two directions are

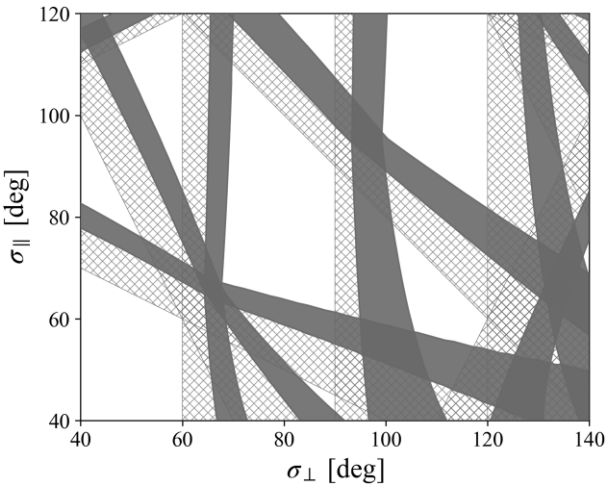

Fig. 6. Stop-band diagram of an equipartitioned bunch. The bunch intensity is the same as in Fig. 5. The rms emittances have been properly adjusted such that the bunch maintains the equipartitioned state everywhere. Coherent core resonances of the second or third order occur within the shaded areas while accompanying tail resonances of twice the order are expected in the hatched area. The tune-shift factors adopted here are identical to those in Fig. 5.

too different. Then, the difference resonances with $n_\perp/n_\parallel = -0.5$ disappear because $\Lambda(n_\perp, n_\parallel)$ is close to zero.

Another example is exhibited in Fig. 6 where the beam is equipartitioned everywhere. We have controlled the ratio of the transverse and longitudinal rms emittances, while keeping the bunch intensity, such that the equipartitioning condition is satisfied over the whole tune space. The stop bands look somewhat narrower than the case in Fig. 5, which is due to a slight reduction of the beam density. Of particular note is the fact that, in addition to the stop band with $(n_\perp, n_\parallel, n') = (1, -2, 0)$, two more synchrobetatron difference resonances with $(n_\perp, n_\parallel, n') = (1, -1, 0)$ and $(2, -1, 0)$ are missing in Fig. 6. As first pointed out in Ref. [27], the condition $\Lambda(n_\perp, n_\parallel) \approx 0$ is automatically met between the transverse and longitudinal degrees of freedom when the bunch is equipartitioned. In fact, combining the equipartitioning condition with $\Lambda(n_\perp, n_\parallel) = 0$, we obtain the relation $n_\perp \eta_\perp \sigma_\perp + n_\parallel \eta_\parallel \sigma_\parallel = 0$, which is close to the coherent resonance line in Eq. (7) with $n' = 0$ because $C_m \approx 1$ for $m \geq 2$. The second-order and third-order resonance bands mentioned above are, therefore, strongly suppressed in an equipartitioned bunch. We, however, stress that this favorable outcome has nothing to do with any thermodynamic processes. The condition in Eq. (6) is more essential and general in terms of difference resonance suppression because it applies even to resonances with $n' \neq 0$ [19].

In the case of a typical circular machine, the operating point does not move during acceleration. Since all stop bands generally shrink as the beam is accelerated to higher energy (see, e.g. Fig. 1 in Ref. [31]), one can avoid all major resonances throughout the whole acceleration process simply by choosing the operating bare tunes within a resonance-free area at injection.

The situation is more complicated in a linear machine. The phase advances of both transverse and longitudinal directions vary, which may result in resonance crossing depending on the initial operating point and lattice design. Unlike in synchrotrons, the widths of stop bands need to be updated in consideration of the energy-dependent shift of the operating point. In an equipartitioned linac design, for instance, the overall picture of the stop-band diagram does not

change much throughout the acceleration process. In that case, one may optimize the operating parameters, viewing the stability map either at the entrance or at the end of the machine.

4. Multiparticle simulations

In Sect. 2, we verified that the simple condition in Eq. (4) can almost precisely reproduce the locations of major stop bands predicted by the KV-based Vlasov theory. We here try to conduct a further test of the new design scheme, employing self-consistent multiparticle simulations with the Gaussian beam, which is much more realistic than the KV beam. Following a previous simulation study [27], the sinusoidal focusing model, instead of the FODO lattice, is taken because of better convergence and some technical reasons. It has been proved that the resonance feature is quite insensitive to which lattice configuration is chosen [15,32]. We have reconfirmed this fact, employing the linearized Vlasov analysis; there is no noticeable difference between the stop bands of the FODO lattice (Figs. 1, 2, and 3) and those of the sinusoidal focusing channel. The focusing force varies sinusoidally in the longitudinal direction as well, bearing the most typical DTL structure in mind (see Fig. 1 in Ref. [27]).

Whenever the beam density is high in phase space, it is extremely important to construct an initial distribution of particles as precisely matched to the external beam focusing potential as possible. The phase-space matching has to be done including the effect from the strong space-charge potential. Otherwise, emittance growth will occur inevitably during the natural self-organization process toward the ideal stationary state (the Debye screening effect) right after the beam is injected into the machine. Such mismatch-induced emittance growth obscures the signatures of weak instabilities, making it difficult to identify the existence of nonlinear coherent resonance bands. In this simulation study, we employed a matching technique originally developed by Lund et al. [27,33]. A pseudo-equilibrium distribution of the Gaussian type was used for each simulation, which can actually minimize the undesired emittance growth irrelevant to resonance unless $\eta_{\perp(\parallel)}$ is too small. According to our past experience, this matching technique works fairly well as long as the tune depression is above, say, around 0.6. A matching error starts to be nonnegligible at a tune depression below 0.5.

Systematic multiparticle simulations were carried out with the PIC code "WARP" [34] at 2000 different operating points over the tune range $40^\circ \leq \sigma_\perp \leq 140^\circ$ in the transverse directions and $40^\circ \leq \sigma_\parallel \leq 120^\circ$ in the longitudinal. The emittance growth after the beam passed through 100 AG focusing periods is color-coded in Figs. 7 and 8 where the initial beam conditions are identical to those assumed, respectively, in Figs. 5 and 6. The largest emittance growth of the three directions is taken at each operating point to determine the color.

Since the intensity and initial rms emittances are fixed in Fig. 7, the bunch is nonequipartitioned at the beginning, except in the vicinity of the operating point $(\sigma_\perp, \sigma_\parallel) = (50^\circ, 25^\circ)$. In Fig. 8, the equipartitioning condition has been met everywhere. These PIC results are consistent with the stop-band diagrams constructed in Sect. 3; all the instability bands foreseen in Figs. 5 and 6, no more and no less, are recognizable. The sum resonance with $(n_\perp, n_\parallel, n') = (1, 2, 1)$ is quite weak but does exist [27]. As theoretically expected, the difference resonance band corresponding to $(n_\perp, n_\parallel, n') = (1, -2, 0)$ is invisible in both cases. In the equipartitioned case (Fig. 8), two more difference resonance bands, those with $(n_\perp, n_\parallel, n') = (1, -1, 0)$ and $(2, -1, 0)$, have disappeared just like in Fig. 6. The effect of these difference resonances depends on how seriously the condition $\Lambda(n_\perp, n_\parallel) = 0$ is broken. In Fig. 9, we have switched the initial emittance ratio $\varepsilon_\perp/\varepsilon_\parallel$ from 1/2 (assumed in Fig. 7) to 2/1 while keeping the

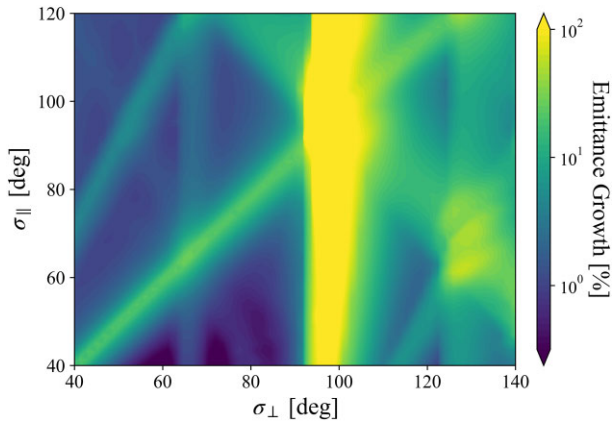

Fig. 7. Result of PIC simulations with the nonequipartitioned setup adopted in Fig. 5. Simple sinusoidal focusing is assumed in all three directions to model the lattice condition of a typical DTL.

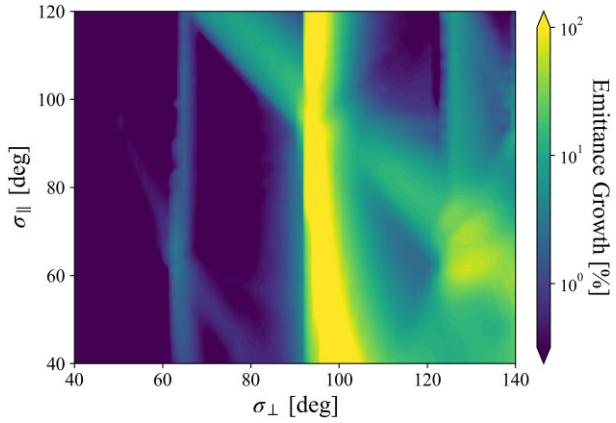

Fig. 8. Result of PIC simulations with the equipartitioned setup adopted in Fig. 6. The lattice condition is the same as assumed in Fig. 7.

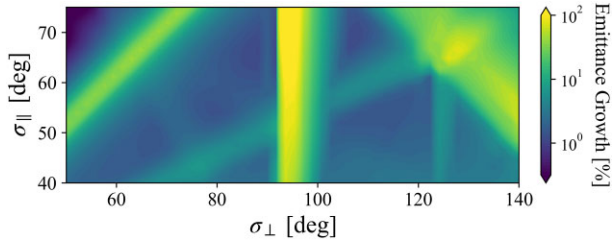

Fig. 9. Result of PIC simulations. The input parameters used here are the same as in Fig. 7 except for the initial rms emittances.

same beam intensity. The difference resonance unobservable in Fig. 7 has now been activated clearly.

5. Application

The self-consistent Vlasov analysis and PIC data in previous sections have shown that the proposed stop-band diagram provides reliable information about the stability of high-intensity hadron bunches. We now try to apply this theory for the optimization of fundamental linac parameters. A couple of different design concepts are considered here as examples and

Table 1. Main parameters of the Alvarez DTL assumed for PIC simulations.

Ion species	H^-
Peak current	50 mA
Operating rf frequency	324 MHz
Initial kinetic energy	3 MeV
Number of unit cells	200
Transverse focusing lattice	FODO
Q-mag core length at 1st cell	40 mm
Bore radius	8 mm
Synchronous rf phase	-30°
Average accelerating field	2.7 MV/m
Transverse rms emittance (normalized)	$0.3\,\pi$mm · mrad

numerically evaluated through WARP simulations assuming an Alvarez-type DTL. The ion species is negative hydrogen (H^-) injected at the kinetic energy of 3 MeV. The operating frequency is set at 324 MHz, the same as the DTL at the J-PARC [35]. Other fundamental parameters are also chosen by reference to the J-PARC design. The main parameters are summarized in Table 1 but, needless to say, the present design approach is never limited to this particular set of numbers. It can readily be applied to any DTLs that accelerate other ion species at other operating frequencies.

The normalized rms emittances of a typical H^- beam from the radio-frequency quadrupole (RFQ) linac at the J-PARC are expected to be $\varepsilon_\perp = 0.220\,\pi$mm · mrad and $\varepsilon_\parallel = 0.295\,\pi$mm · mrad (Y. Liu, personal communication). The beam quality is deteriorated to some degree in the medium-energy beam transport between the RFQ linac and the Alvarez DTL. A recent simulation study indicates that the transverse emittance grows to around $\varepsilon_\perp = 0.3\,\pi$mm · mrad at the entrance of the DTL [36]. This number is adopted in all of the following PIC simulations. As for the longitudinal emittance, we take a few different values a bit greater than $0.295\,\pi$mm · mrad.

The average gap field ranges from 2.5 MV/m to 2.9 MV/m in the J-PARC DTL where H^- ions are accelerated from 3 MeV to 50 MeV in 27.12 m [6]. The synchrotron phase advance $\sigma_\parallel$ is significantly below 90° at this level of acceleration rate; specifically, it is about 31.9° at 3 MeV with the accelerating field of 2.7 MV/m and monotonically decreases as the beam gains energy. If $\sigma_\perp$ is kept below 60°, only three low-order stop bands need particular attention, namely, those with $(n_\perp, n_\parallel, n') = (1, -1, 0)$, $(2, -1, 0)$, and $(1, -2, 0)$. It is thus relatively easy to find a resonance-free area in tune space. Once $\sigma_\perp$ goes beyond 60°, it becomes more and more difficult to avoid resonance crossing during acceleration; as we can see from Figs. 5. and 6, the low synchrotron-tune area ($\sigma_\parallel \lesssim 60^\circ$) is mostly covered by low-order coherent bands and potentially dangerous incoherent-resonance domains.

5.1. *Design A:* $\eta_\perp\sigma_\perp/\eta_\parallel\sigma_\parallel \approx const.$

Let us start with the case where the ratio of the effective phase advances in the transverse and longitudinal directions is maintained from the entrance to the exit of the linac. Such a design is of practical interest because the equipartitioning condition requires the machine designer to adjust this ratio to a proper value. When the effective tune ratio $\eta_\perp\sigma_\perp/\eta_\parallel\sigma_\parallel$ is equalized to the emittance ratio $\varepsilon_\parallel/\varepsilon_\perp$ throughout the linac, such a machine design is called "equipartitioned." In reality, however, it is very difficult to control the initial emittance ratio. There exist a variety of

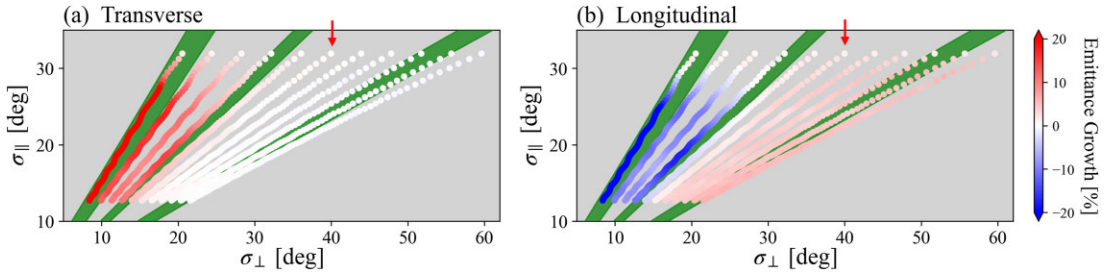

Fig. 10. Results of PIC simulations assuming a typical DTL structure. The tune trajectories of 11 independent PIC simulations are plotted with color-coded dots that represent the emittance growth rate (a) in the transverse direction and (b) in the longitudinal direction. The ratio of the effective betatron and synchrotron phase advances, i.e. $\eta_\perp\sigma_\perp/\eta_\parallel\sigma_\parallel$, is kept constant along each dotted line. The equipartitioning condition has been approximately met in the simulation run indicated by a red arrow. The linear ($m = 2$) and lowest-order nonlinear ($m = 3$) coherent stop bands expected from the theory in Sect. 3 are superimposed for reference.

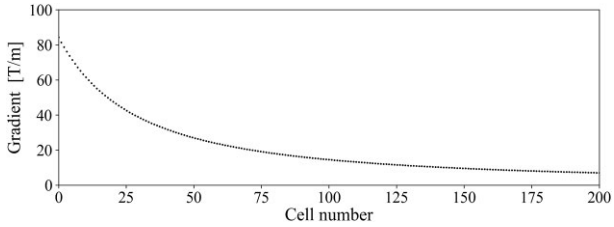

Fig. 11. Variation of the quadrupole-field gradient along the linac when the phase advances at the first cell are $(\sigma_\perp, \sigma_\parallel) = (40.0^\circ, 31.9^\circ)$. The core length of a quadrupole magnet has become longer at the same rate as the unit cell length.

inevitable error sources that affect the condition of an incident beam, especially at high space-charge intensity. A question of practical importance is what happens if $\varepsilon_\parallel/\varepsilon_\perp$ differs from the ideal value assumed in the design stage of a linac.

Figure 10 shows the results of 11 separate PIC simulation runs in which the initial longitudinal emittance is set at $0.4\,\pi$mm · mrad, a bit greater than the transverse value. The DTL considered here accelerates the H^- beam up to 90.9 MeV in 46.7 m. At 3 MeV, $\sigma_\parallel$ is 31.9° with the parameters listed in Table 1. $\sigma_\perp$ is controllable by changing the field gradient of the quadrupole magnets. Each dotted line in Fig. 10 represents the trajectory of the DTL operating point starting from a certain value of $\sigma_\perp$. The color of each dot, plotted for every FODO period, reflects the rate of emittance growth. We have chosen 11 different initial values of $\sigma_\perp$ over the range $20^\circ \lesssim \sigma_\perp \lesssim 60^\circ$ with $\sigma_\parallel$ fixed at 31.9°.

As $\sigma_\parallel$ decreases with increasing beam energy, the quadrupole gradient must be adjusted to keep the ratio $\eta_\perp\sigma_\perp/\eta_\parallel\sigma_\parallel$. The tune depressions, determined by solving the rms envelope equations, are a function of the operating phase advances. Iterative calculations are thus necessary to find the proper gradient at every cell. The tune depression considerably varies during acceleration, depending on the initial operating point; in the case of Fig. 10, it ranges from 0.50 to 0.74 in the transverse direction and from 0.75 to 0.54 in the longitudinal direction. The gradients of the quadrupole focusing fields vary as depicted in Fig. 11 when the initial operating point is chosen at $(\sigma_\perp, \sigma_\parallel) = (40.0^\circ, 31.9^\circ)$. We have changed the core lengths of 200 quadrupoles gradually, at the same rate as the increase of the cell length. In the J-PARC DTL, quadrupole magnets of seven different core lengths are installed in the drift tubes [35].

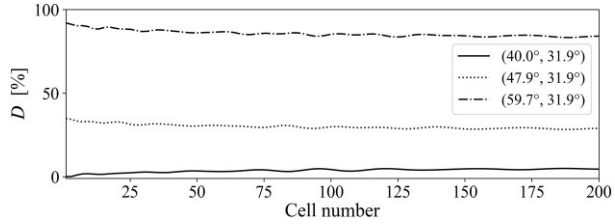

Fig. 12. Degree of deviation from the equipartitioned state. The D-value defined in Eq. (10) is evaluated for three cases in Fig. 10 where the starting phase advances are $(\sigma_\perp, \sigma_\parallel) = (40.0^\circ, 31.9^\circ)$ (equipartitioned), $(47.9^\circ, 31.9^\circ)$, and $(59.7^\circ, 31.9^\circ)$.

The three green bands in Fig. 10 indicate the regions of possible low-order coherent resonances predicted by the theory in Sect. 3. In the present case, the stop-band distribution does not change much during acceleration, which is due to a large shift of the operating point. The widths of the stop bands in Fig. 10 are defined with the parameters at the linac entrance. A clear emittance exchange between the transverse and longitudinal degrees of freedom takes place when the operating point moves along a difference resonance band with $(n_\perp, n_\parallel, n') = (1, -1, 0)$ or with $(n_\perp, n_\parallel, n') = (2, -1, 0)$. Since $\varepsilon_\perp < \varepsilon_\parallel$ at the entrance, the emittance flows from the longitudinal to the transverse direction. Interestingly, the difference resonance with $(n_\perp, n_\parallel, n') = (1, -2, 0)$ has no serious effect, unlike the other two. The same tendency has been found also in an earlier simulation study [27] and even experimentally [28]. This resonance is certainly present as confirmed in Fig. 9 but much less active with the parameter setup adopted here.

Another important fact immediately understood from Fig. 10 is that the equipartitioned linac design is not the only solution to guarantee the best beam quality. The equipartitioning condition indeed widens the usable operating area in tune space (as theoretically explained in Ref. [27]), but we have more flexibility in choosing the basic design parameters. In all 11 simulation results plotted in Fig. 10, the emittance ratio $\varepsilon_\parallel/\varepsilon_\perp$ is equal to 0.4/0.3 initially, which means that the equipartitioning condition is met only when $\eta_\perp\sigma_\perp/\eta_\parallel\sigma_\parallel \approx 1.33$. The operating point close to this particular case is indicated by a red arrow in Fig. 10, showing no emittance growth until the exit. We, however, see several other cases with no serious degradation in beam quality. For quantitative discussion, let us introduce the parameter

$$D \equiv \left| \frac{\eta_\perp\sigma_\perp}{\eta_\parallel\sigma_\parallel} \cdot \frac{\varepsilon_\perp}{\varepsilon_\parallel} - 1 \right| \tag{10}$$

to measure the deviation from the equipartitioned state. The D-value along the arrowed operating line in Fig. 10 actually stays near zero as illustrated in Fig. 12. Two more examples added to Fig. 12 are based on the design parameters when the starting point is put either at $(\sigma_\perp, \sigma_\parallel) = (47.9^\circ, 31.9^\circ)$ or at $(59.7^\circ, 31.9^\circ)$. While these two cases are far from the equipartitioned design, only little emittance growth has occurred in Fig. 10.

We now repeat the 11 simulations after changing the longitudinal rms emittance from $0.4\,\pi$ mm · mrad to $0.3\,\pi$ mm · mrad. All the other parameters are identical to what we assumed in Fig. 10. Since the current is maintained at 50 mA with $\varepsilon_\parallel$ reduced by 25%, the beam density has become higher in phase space. For instance, the tune depressions at $(\sigma_\perp, \sigma_\parallel) = (32.2^\circ, 31.9^\circ)$ decrease from $(\eta_\perp, \eta_\parallel) = (0.60, 0.66)$ to $(0.59, 0.59)$. In the previous case (Fig. 10), we observed a clear synchrobetatron coupling effect caused by the difference resonance with $(n_\perp, n_\parallel, n') = (1, -1, 0)$ when starting from this operating point. Such a signature of instability is no longer

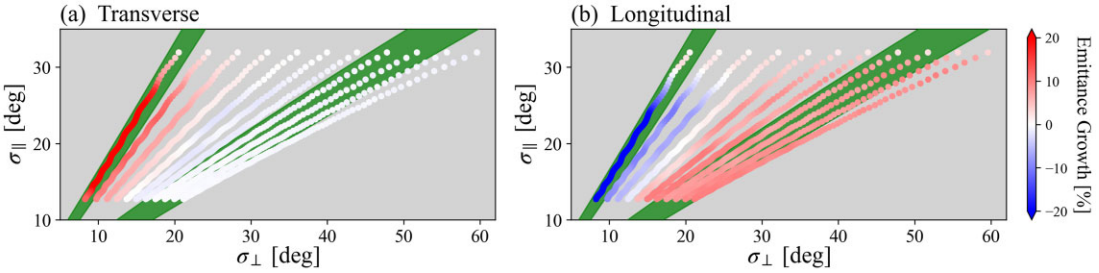

Fig. 13. Results of PIC simulations. Fundamental parameters are the same as in the case of Fig. 10, except for the initial longitudinal rms emittance being reduced from $0.4\,\pi$ mm · mrad to $0.3\,\pi$ mm · mrad here. Owing to the equalization of the transverse and longitudinal emittances, the linear difference resonance band with $(n_\perp, n_\parallel, n') = (1, -1, 0)$ has disappeared.

identified in Fig. 13 despite the fact that the beam is denser. The second-order stop band has been deactivated by the equalization of the transverse and longitudinal emittances at injection.

Similarly to the case in Fig. 10, the third-order difference resonance with $(n_\perp, n_\parallel, n') = (1, -2, 0)$ is not severe. Weak longitudinal emittance growth detected in Fig. 13 with a high starting $\sigma_\perp$ is due largely to the initial mismatch rather than overlapping with the difference resonance. A similar slight increase of the longitudinal emittance (less than 6%) can also be seen in Fig. 10(b) at high $\sigma_\perp$. As noted in the last section, a certain amount of emittance growth is inevitable even with a pseudo-equilibrium distribution when the tune depression is too small. Under the operating condition in Fig. 13, $\eta_\parallel$ is below 0.5 already at the first cell and eventually reaches 0.4 after acceleration when the starting $\sigma_\perp$ exceeds 50°. The longitudinal emittance jumps by roughly 10% within the first 10 cells and then comes into a sort of plateau. In the transverse degrees of freedom, almost nothing has happened, which implies that the coupling resonance should not be the primary source of this weak longitudinal instability.

5.2. *Design B: $\sigma_\perp \approx const.$*

The second case of interest is the parameter setting that makes the betatron phase advance constant along the machine. In Design A, $\sigma_\perp$ monotonically decreases, resulting in the increase of the transverse beam size. For instance, the rms radius of the matched beam under the equipartitioned operation in Fig. 10 grows from about 1.1 mm at the entrance to about 1.9 mm at the exit. We can suppress such beam-size growth by maintaining $\sigma_\perp$, which may be advantageous for beam-loss minimization. The rms radius of the output beam in the aforementioned case can be made roughly 1.0 mm instead of 1.9 mm.

We again performed PIC simulations starting from 11 different operating points, as shown in Fig. 14. Just like in Figs. 10 and 13, the initial value of $\sigma_\perp$ is varied with $\sigma_\parallel$ kept at 31.9°. The rms emittances at the linac entrance are $\varepsilon_\perp = 0.3\,\pi$ mm · mrad and $\varepsilon_\parallel = 0.4\,\pi$ mm · mrad, identical to the values in Fig. 10. The stop-band distribution remains unchanged then. Since $\sigma_\parallel$ goes down to about 12.7° vertically in the stability chart, the operating point crosses the strong linear synchrobetatron resonance with $(n_\perp, n_\parallel, n') = (1, -1, 0)$ unless it is initially positioned on the right side of the stop band. When $\sigma_\perp$ is close to 20° at injection, the operation starts inside the third-order stop band with $(n_\perp, n_\parallel, n') = (2, -1, 0)$, which gives rise to emittance exchange in the early stage of acceleration. The influence of the second-order difference resonance is also visible, but its effect is relatively weak in the range $\sigma_\parallel \gtrsim 30°$. This is simply because the operating point traverses the linear stop band only within a few FODO periods. As readily understood

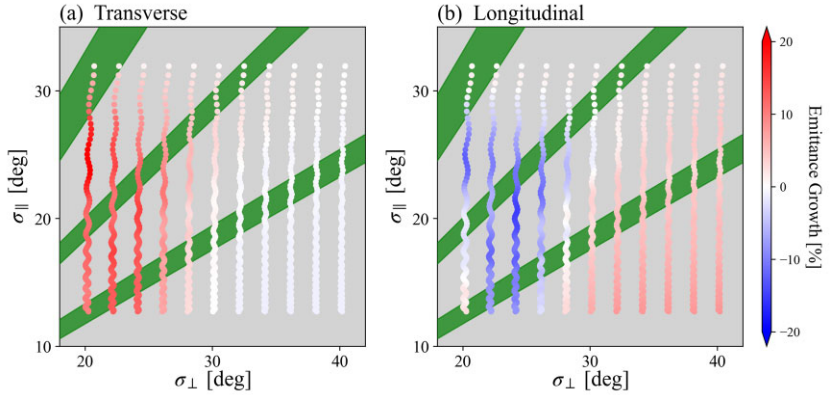

Fig. 14. Results of PIC simulations in the case where the bare betatron phase advance is kept constant through the linac. The initial rms emittances are the same as assumed in Fig. 10; namely, $\varepsilon_\perp = 0.3\,\pi\,\mathrm{mm}\cdot\mathrm{mrad}$ and $\varepsilon_\parallel = 0.4\,\pi\,\mathrm{mm}\cdot\mathrm{mrad}$ at injection.

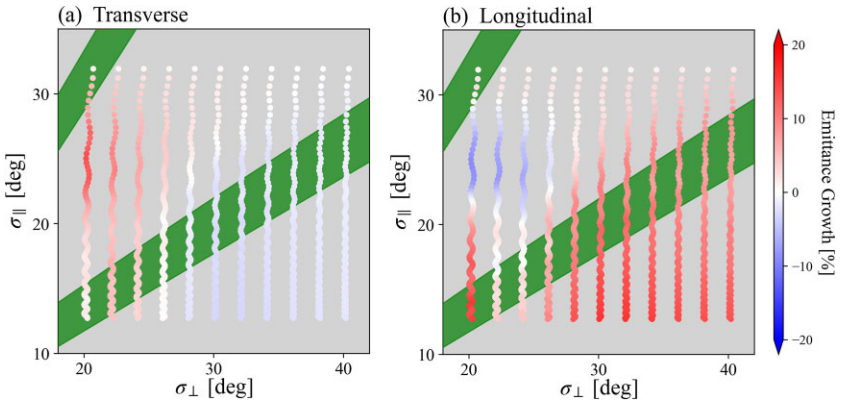

Fig. 15. Results of PIC simulations. The longitudinal rms emittance is reduced to $\varepsilon_\parallel = 0.3\,\pi\,\mathrm{mm}\cdot\mathrm{mrad}$. Other parameters are identical to those assumed in Fig. 14.

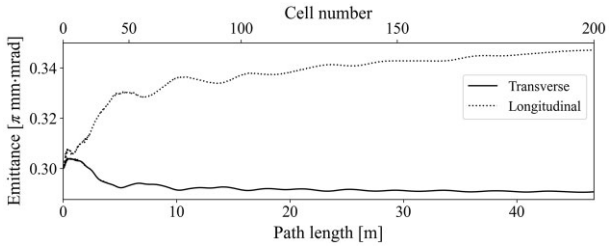

Fig. 16. Evolution of rms emittances along the operating line with $\sigma_\perp = 30^\circ$ in Fig. 15.

from the density of colored dots (plotted for every FODO period), the moving speed of the operating point in the chart is faster near the entrance of the machine.

We recognize a slight increase of $\varepsilon_\parallel$ that appears to be induced by the stop band with $(n_\perp, n_\parallel, n') = (1, -2, 0)$. As seen in Fig. 15, this effect is somewhat enhanced when the transverse and longitudinal emittances are equalized initially. The PIC results indicate a clear signature of an emittance flow between the transverse and longitudinal degrees of freedom. The observed flow is not due to the linear coupling resonance because it is inactive under the condition $\varepsilon_\perp = \varepsilon_\parallel$. Figure 16 shows an example of the emittance evolution when the operating point

is initially put at $(\sigma_\perp, \sigma_\parallel) = (30.0^\circ, 31.9^\circ)$. The amount of the longitudinal emittance increase is roughly twice as large as that of the transverse emittance decrease, suggesting that the driving source is most likely the third-order difference resonance $\sigma_\perp - 2\sigma_\parallel = 0$.

The impact of the nonlinear resonance with $(n_\perp, n_\parallel, n') = (1, -2, 0)$ is relatively small, compared with the other two stop bands plotted in Fig. 14. Even so, it is advisable to avoid crossing this line because third-order error fields can directly drive it, thus enhancing the instability. Mechanical errors are inevitable in any real machines, so the actual impact of this stop band is probably stronger than the numerical expectations here.

6. Summary

We have studied a simple design guideline applicable to both linear and circular hadron accelerators. The resonance theory reviewed in Sect. 2, which leads to stop-band diagrams as in Sect. 3, can naturally explain the basic features of beam instability revealed by self-consistent multiparticle simulations in Sect. 4. According to the present theory, low-order coherent core resonances or incoherent tail resonances adjacent to a core resonance band are responsible for the emittance growth observed in the simulations. The proposed new design scheme allows for quick optimization of fundamental machine parameters; all one has to do is simply to keep the operating point out of major stop bands visualized in the conventional tune space.

Unlike in typical circular machines, the operating betatron and synchrotron phase advances of a linac generally vary as the beam is accelerated. It is thus essential to find a sufficiently wide resonance-free area in tune space. In this respect, choosing both phase advances below 60° should be advantageous. In the present examples referring basically to the J-PARC DTL design, a primary cause of dangerous resonance crossing is a change in $\sigma_\parallel$ during acceleration that moves the operating point downward in tune space. The performance of a high-intensity hadron linac can be improved by minimizing this movement of the operating point to avoid low-order resonance crossing.

When $\sigma_\parallel$ is lower than 60° (as is mostly the case with normal-conducting linacs), too high a transverse phase advance is probably risky; $\sigma_\perp$ below 60° seems most reasonable as can be seen from the stop-band diagrams in Sect. 3 as well as the PIC results in Sect. 4. In such a low-tune range, we encounter three major stop bands with $(n_\perp, n_\parallel, n') = (1, -1, 0)$, $(2, -1, 0)$, and $(1, -2, 0)$. All of them can be eliminated by requiring fundamental design parameters to fulfill the equipartitioning condition, i.e. $\varepsilon_\parallel/\varepsilon_\perp = \eta_\perp\sigma_\perp/\eta_\parallel\sigma_\parallel$. This is a clear advantage of the equipartitioned linac design, but there is no guarantee that the actual emittance ratio at the linac entrance agrees with the ideal design value. In fact, considerable emittance growth is expected in the short matching section before the Alvarez linac at J-PARC [36], which may make the original design parameters no longer well equipartitioned. Practical problems like this more or less arise in all machines. At high space-charge density, phase-space matching from one linac structure to another is extremely difficult even in computer simulations. The sudden emittance growth observed in a high-$\sigma_\perp$ range of Fig. 13(b) is a good example.

The present study has clearly demonstrated that the degradation of beam quality can be minimized even without the equipartitioning condition being satisfied. The equipartitioned linac design is certainly beneficial to emittance preservation, but what really matters is the condition in Eq. (6) that has nothing to do with the thermodynamic equilibrium. We can deactivate all difference resonances with a specific $|n_\parallel/n_\perp|$ by setting the emittance ratio $\varepsilon_\parallel/\varepsilon_\perp$ close to this

rational number. In any case, it is theoretically possible to avoid severe emittance growth or emittance transfer even in a linac far from the equipartitioned design.

Acknowledgements
The authors are indebted to Dr. K. Kojima for his assistance in an early stage of this research.

Funding

This work is supported in part by Japan Society for the Promotion of Science (JSPS) KAKENHI Grant No. 22K12671.

References

[1] M. Reiser, Theory and design of charged particle beams. New York: John Wiley & Sons; 2008, and references therein.
[2] T. P. Wangler, RF linear accelerators. New York: John Wiley & Sons; 1998, and references therein.
[3] I. Hofmann, L. J. Laslett, L. Smith, and I. Haber, Part. Accel. **13**, 145 (1983).
[4] J. Struckmeier, J. Klabunde, and M. Reiser, Part. Accel. **15**, 47 (1984).
[5] R. A. Jameson, IEEE Trans. Nucl. Sci. **28**, 2408 (1981).
[6] M. Ikegami, Prog. Theor. Exp. Phys. **2012**(1), 02B002 (2012).
[7] Y. Kondo, T. Morishita, and R. A. Jameson, Phys. Rev. Accel. Beams **22**, 120101 (2019).
[8] I. Hofmann, Phys. Rev. E **57**, 4713 (1998).
[9] Z.-J. Wang et al., Phys. Rev. Accel. Beams **27**, 010101 (2024).
[10] C. Zhang, Phys. Rev. Accel. Beams **25**, 034201 (2022).
[11] B. Yee-Rendon, Y. Kondo, F. Maekawa, S. Meigo, and J. Tamura, Phys. Rev. Accel. Beams **24**, 120101 (2021).
[12] A. Pathak, S. Roy, S. Rao, and S. Krishnagopal, Phys. Rev. Accel. Beams **23**, 090101 (2020).
[13] X. J. Yin et al., Phys. Rev. Accel. Beams **19**, 010402 (2016).
[14] Z. Li et al., Phys. Rev. Accel. Beams **16**, 080101 (2013).
[15] K. Ito, H. Okamoto, Y. Tokashiki, and K. Fukushima, Phys. Rev. Accel. Beams **20**, 064201 (2017).
[16] H. Okamoto and K. Yokoya, Nucl. Instrum. Meth. A **482**, 51 (2002).
[17] E. D. Courant and H. S. Snyder, Ann. Phys. (N.Y.) **3**, 1 (1958).
[18] W. Montague, Fourth-order coupling resonances excited by space-charge forces in a synchrotron. Geneva: CERN; 1968. Report No.: CERN/ISR/68-38.
[19] K. Kojima, H. Okamoto, and Y. Tokashiki, Phys. Rev. Accel. Beams **22**, 074201 (2019).
[20] K. Kojima, H. Okamoto, and Y. Tokashiki, Phys. Rev. Accel. Beams **23**, 028002 (2020).
[21] H. Okamoto, M. Aoki, C. Ichikawa, K. Kojima, T. Kurauchi, and Y. Yamane, J. Instrum. **15**, P07017 (2020).
[22] H. Hotchi et al., Phys. Rev. Accel. Beams **20**, 060402 (2017).
[23] F. J. Sacherer, Transverse space-charge effects in circular accelerators [Ph.D. thesis]. Berkeley (CA): Lawrence Radiation Laboratory; 1968. Report No.: UCRL-18454. October 30, 1968.
[24] C. Li and R. A. Jameson, Phys. Rev. Accel. Beams **21**, 024204 (2018).
[25] Y. Tokashiki, Theoretical study of collective resonance instability in high-intensity beams [Master thesis], Graduate School of Advanced Sciences of Matter (AdSM), Hiroshima University; 2017.
[26] F. J. Sacherer, IEEE Trans. Nucl. Sci. **NS-18**, 1105 (1971).
[27] Y. Yamane, H. Okamoto, and K. Kojima, Phys. Rev. Accel. Beams **24**, 084201 (2021).
[28] M. Goto, C. Ichikawa, K. Ito, K. Kojima, and H. Okamoto, Phys. Rev. Accel. Beams **25**, 054201 (2022).
[29] I. M. Kapchinskij and V. V. Vladimirskij, Limitations of proton beam current in a strong focusing linear accelerator associated with the beam space charge, Kowarski L., editor. Proceedings of the 2nd International Conference on High-Energy Accelerators and Instrumentation, HEACC 1959. September 14–19, 1959; CERN, Geneva, Switzerland. Geneva: CERN; 1959, p. 274.
[30] R. L. Gluckstern, Oscillation modes in two-dimensional beams. In: M. R. Tracy, editor. Proceedings of the 1970 Linear Accelerator Conference. September 28–October 2, 1970. Batavia (IL): Fermilab; 1970, p. 811.

[31] K. Kojima and H. Okamoto, Phys. Rev. Accel. Beams **25**, 024201 (2022).
[32] K. Fukushima, K. Ito, H. Okamoto, S. Yamaguchi, K. Moriya, H. Higaki, T. Okano, and S. M. Lund, Nucl. Instrum. Meth. A **733**, 18 (2014).
[33] S. M. Lund, T. Kikuchi, and R. C. Davidson, Phys. Rev. ST Accel. Beams **12**, 114801 (2009).
[34] D. P. Grote, A. Friedman, G. Craig, I. Haber, and W. Sharp, Nucl. Instrum. Meth. A **464**, 563 (2001).
[35] High-intensity Proton Accelerator Project Team, Accelerator Technical Design Report for High-intensity Proton Accelerator Facility Project, J-PARC, Y. Yamazaki, editor. Japan Atomic Energy Research Institute, 2003. Report No.: JAERI-Tech 2003-44, KEK Report 2002-13.
[36] M. Chimura, H. Harada, and M. Kinsho, Prog. Theor. Exp. Phys. **2022**(6), 063G01 (2022).